Diffusion of Si impurities in Ni under stress: A first-principles study

Thomas Garnier,[1] Venkateswara R. Manga,[1,2] Pascal Bellon,[1] and Dallas R. Trinkle[1]

[1]*Department of Materials Science and Engineering, University of Illinois at Urbana-Champaign, Urbana, Illinois 61801, USA*

[2]*Department of Materials Science and Engineering, University of Arizona, Tucson, Arizona 85721, USA*

We perform a first-principles study of the effect of strain on the migration of Si atoms in Ni. For that purpose, migration barriers are computed using the nudged elastic band method and attempt frequencies are computed using the direct force method. Good agreement is found with tracer diffusion experiments. We used the elastic dipole model to calculate effects of strain on migration barriers by performing calculations on unstrained cells, therefore reducing significantly the computing time. We validate this approach by comparing results with migration barriers calculated on strained cells and obtain an excellent agreement up to a strain of 1%. Computing all the jump frequencies in the neighborhood of Si solutes, the effect of strain is found to be nearly independent of the relative position of the solute atom. A simple elastic analysis models the changes in the vacancy jump with strain; this correlates with the changes in geometry for the "cage" of atoms surrounding the hopping atom at the saddle point.

I. INTRODUCTION

Irradiation of alloys produces vacancies and interstitial atoms in the bulk of the material [1]. These point defects are mobile at finite temperature, and their elimination at sinks such as dislocations, grain boundaries, or free surfaces induces a flux of point defects within the material [2]. These point defects also activate the diffusion of solute atoms. Furthermore, atomic fluxes are coupled to the point defect fluxes [3–5]. These flux couplings can induce a depletion or a segregation of solute atoms in the neighborhood of the defect sinks [6,6–8]. Radiation-induced segregation can lead to the precipitation of solute-rich phases near these sinks [9,10], as is the case for solid solution of Si in Ni [7,8,11]. In a substitutional alloy, the description of flux coupling requires an accurate knowledge of the jumps of the vacancy around the solute [3,4]. The jump frequencies can be computed using density functional theory (DFT) calculations [12–16] and their results incorporated into atomic kinetic Monte Carlo (AKMC) simulations [12,13,16] or into a mean-field model [14,15] to provide the Onsager matrix.

Stress and atomic diffusion closely affect each other. Sinks such as dislocations and grain boundaries generate a stress field that modifies diffusion properties in their neighborhood. Stress affects diffusion both from a thermodynamic and a kinetic point of view, through the driving force and the Onsager matrix. Earlier work addressed the thermodynamic aspect of the problem [17–20]. Regarding the kinetic aspects, the symmetry of the saddle point configuration is the key element of the stress-induced symmetry breaking [21–23]. Recent simulations show that both aspects need to be considered to achieve accurate simulations of microstructure evolution [24] or to model diffusion around a dislocation [25,26].

In a previous publication [27], we investigated the effect of the strain field induced by an edge dislocation on the Si flow in Ni. Here, we detail how DFT calculations can be used to obtain the effect of strain on the atomic-scale diffusion properties in the case of Si-vacancy-mediated diffusion in Ni. By performing DFT calculations on strained and unstrained cells, we show that in the case of the Si impurities in Ni,

the effect of strain on the jump frequencies can be obtained without requiring systematic calculations on the strained cell by using the elastic dipole description [20,28,29]. Moreover, in the case of the Ni(Si) system, the strain effect appears to be mostly independent of the type of jump. The methods used to compute the effect of strain on the jump frequencies and the DFT calculations are presented in the first section. Next, the results obtained in the case of the Ni(Si) alloy are presented and discussed. Finally, the results are compared to a simple elastic model proposed in Ref. [30].

II. METHODOLOGY

A. Atomic-scale diffusion

At the atomic scale, diffusion is a succession of thermally activated events, each of them corresponding to an atomic jump. The frequency of those events depends on the local chemical environment, and the number of different events—and thus the number of different frequencies—depends on the crystal structure and the migration mechanism considered. We consider the case of vacancy-mediated diffusion in the dilute limit. The range of the vacancy-solute binding energy determines the number of events to consider. Our preliminary work showed that binding energies between Si atoms and vacancies extend up to the third-nearest-neighbor sites and these interactions are detailed in Sec. II B. In an unstressed fcc structure where a vacancy can only move to the nearest-neighbor (NN) sites and interacts with the solute atoms up to the third-NN sites, there are 16 unique geometries of the triplet-jumping atom-vacancy solute to be determined.

Following the notation introduced in Ref. [3], these 16 frequencies can be written under the form $w_{abc}^{(\zeta)}$, where a designates the vacancy-jumping atom vector symmetry class, b the solute-jumping atom symmetry class, and c the vacancy-solute symmetry class, while $\zeta = 0$ for jumps in the bulk, $\zeta = 1$ for jumps from a site in interaction with a solute toward another one, $\zeta = 2$ for a vacancy-solute exchange, $\zeta = 3$ for a dissociation exchange, and $\zeta = 4$ for an association jump. Using the NN distances for a, b, and c the 16 frequencies are

FIG. 1. Vacancy jump frequencies in a dilute fcc binary alloy with third-nearest-neighbor interactions. Arrows indicate the direction of the jumps. The solute atom is represented by a filled circle, and the numbers on lattice sites indicate the distance from the solute atom site while an ∞ indicates sites beyond the range of the interactions. Names of the return jumps have been omitted for the sake of clarity. In all cases, the reverse jump of $w_{abc}^{(1)}$ is $w_{acb}^{(1)}$, and for $w_{ab\infty}^{(4)}$ is $w_{a\infty b}^{(3)}$.

FIG. 2. Exchange of an atom (in black) with a neighboring vacancy represented by a square along the (110) direction in a fcc lattice. The atoms forming the cage around the saddle point are shown in gray.

written $w_1^{(0)}$, $w_1^{(2)}$, $w_{111}^{(1)}$, $w_{121}^{(1)}$, $w_{112}^{(1)}$, $w_{131}^{(1)}$, $w_{113}^{(1)}$, $w_{132}^{(1)}$, $w_{123}^{(1)}$, $w_{133}^{(1)}$, $w_{1\infty1}^{(3)}$, $w_{1\infty2}^{(3)}$, $w_{1\infty3}^{(3)}$, $w_{11\infty}^{(4)}$, $w_{12\infty}^{(4)}$, and $w_{13\infty}^{(4)}$. They are numbered from 0 to 15 in that order (see Table III) and are illustrated in Fig. 1.

Using Vineyard's harmonic transition state equation [31], the frequency $w_{abc}^{(\zeta)}$ can be written as the product of an attempt frequency $\nu_{abc}^{(\zeta)}$ and the exponential of the product of a migration barrier energy $E_{abc}^{\mathrm{mig},(\zeta)}$ and the inverse thermodynamic temperature $\beta = (k_B T)^{-1}$:

$$w_{abc}^{(\zeta)} = \nu_{abc}^{(\zeta)} e^{-\beta E_{abc}^{\mathrm{mig},(\zeta)}}. \qquad (1)$$

In the following, the dependencies of ν and E^{mig} on $\zeta, a, b,$ and c will be omitted when no confusion is possible. As detailed in Sec. II B, DFT calculations can provide ν and E^{mig} for each frequency.

The effect of strain on a given jump depends on the symmetry of the configurations involved in this jump. In the initial configuration of the atomic exchange in bulk Ni (corresponding to $w_1^{(0)}$), a vacancy on a site of the fcc lattice does not lower the cubic symmetry. However the saddle point configuration breaks the cubic symmetry. This situation is illustrated in Fig. 2, which shows an exchange along the [110] direction, where the saddle point breaks the symmetry between the $\langle 100 \rangle$ directions. The presence of a solute atom in the neighborhood also breaks symmetries of the initial and final configurations. Thus in the presence of a strain field, the different variants of each of the 16 types of atomic jumps are differentiated and the 16 frequencies are split into a number of frequencies that depends on the symmetries respected by both the initial configuration and the saddle point.

In the linear limit, the effect of strain is the superposition of the effect of each of its components on the saddle point and the initial configuration. Hence in that limit, the independent knowledge of the effect of each component of the strain tensor is sufficient to describe the effect of any strain tensor. Hence, using cubic symmetry, we investigate the effect of elementary uniaxial and shear strain on the different frequencies of the original fcc structure.

B. DFT calculations

The migration barrier and the attempt frequency of each jump are obtained from first-principles calculations. We used the Vienna Ab initio Simulation Package (VASP), a plane wave DFT code [32]. Non-spin-polarized calculations are performed with Vanderbilt ultrasoft pseudopotentials using respectively an Ar and Ne core for Ni and Si atoms, within the local density approximation [33] using the parametrization by Perdew and Zunger [34]. A plane wave cutoff energy of 420 eV converged to 1 meV/atom is used in all calculations. Preliminary calculations were performed using a 32-atom $2 \times 2 \times 2$ supercell for the calculation and a Γ-centered k-point mesh of $12 \times 12 \times 12$ with a Methfessel-Paxton smearing of 0.1 eV converged to 1 meV/atom. As the third-nearest-neighbor solute-vacancy binding energy represents 40% of the first-nearest-neighbor binding energy, its effect could not be neglected beforehand. In order to consider these third-nearest-neighbor interactions, a 108-atom $3 \times 3 \times 3$ supercell is used with a $8 \times 8 \times 8$ k-point mesh to minimize interactions between periodic images. The configurations are relaxed until forces are below 5 meV/Å. Note that we have chosen non-spin-polarized calculations for Ni in order to reproduce the correct high-temperature nonmagnetic state. The vacancy formation energy depends on the magnetic state; in the current case $E^f = 1.63$eV was found. In comparison, a preliminary calculation in the GGA approximation provided a vacancy formation energy $E^f = 1.381$eV. As experiments provide results ranging between 1.45eV and 1.80eV [35], the LDA approximation was preferred to the GGA. The large disparity between the GGA *ab initio* value and the experimental value is well known and largely due to surface effects, an effect which has been studied in detail in Refs. [36,37].

The migration barriers are obtained from the climbing-image nudged elastic band (NEB) method. The difference between the energy of the transition state and the energy of the original configuration at fixed volume and cell shape provides the migration enthalpy. A single intermediate image is computed [38] between the initial and the final configuration, for which forces along the path are negated while components perpendicular to the path are unchanged. Restoring forces are checked to ensure that a first-order saddle point is found.

The attempt frequency can be written as a product of the phonon frequencies [31]. Let x_j and x_k be two of the $3N$ degrees of freedom of a system of N atoms, m_j and m_k the mass of the related atoms. To each positive eigenvalue E_i of the mass-weighted Hessian $m_j^{1/2} H_{jk} m_j^{1/2}$, a phonon frequency ν_i is associated, with $\nu_i^2 = E_i$. The stability of an equilibrium position ensures that all eigenvalues of the Hessian are positive. However, in the saddle point configuration, a negative eigenvalue is associated with the unstable mode. The attempt frequency is the product of all the real frequencies in the initial configuration (ν_p^0) divided by the product of all real frequencies in the saddle point configuration ($\nu_q^\dagger$):

$$\nu = \frac{\prod_p^{3N-3} \nu_p^0}{\prod_q^{3N-4} \nu_q^\dagger}. \tag{2}$$

In this work, the phonon calculations are performed by using the direct force constant method [39,40] as implemented in the Alloy Theoretic Automated Toolkit (ATAT) [41,42]. A previous study considered the convergence of the attempt frequencies with the number of modes for the Ni(Si) system [27]. A 64-atom supercell with a k-point mesh of $2 \times 2 \times 2$ was used for these calculations. It showed that considering only the modes associated with the displacements of the hopping atom provides a reasonable approximation of the converged value. As a consequence, the values provided here correspond to calculation based on the modes of the hopping atom only, computed in a 108 atom $3 \times 3 \times 3$ cell.

Energy minimization of a pure nickel cubic cell with respect to the volume leads to a lattice parameter a of 3.43 Å. One can note that this value is 3% lower than the experimental value 3.524 Å [43]. The effect of strain on the migration barrier is investigated by performing simulations using the relaxed cubic cell with the lattice parameter $a = 3.43$ Å, as well as on strained geometries described in the Appendix.

C. Description of point defects in elastic theory

Point defects and their migration can be considered within the framework of elastic theory [20,29]. The energy variation ΔE^{el} induced by a homogeneous strain tensor $\underline{\varepsilon}$ of a system of volume V can be written

$$\Delta E^{\text{el}} = \sum_{i,j} V \sigma_{ij} \varepsilon_{ij}, \tag{3}$$

where $\underline{\sigma}$ is the stress tensor of the system. In elasticity theory, a point defect is described by a second-rank tensor P_{ij} usually called "dipole tensor" and a fourth rank tensor $\mathfrak{M}_{ijkl}$, the diaelastic polarizability [18,20,29]. These tensors provide the excess elastic energy $\Delta E(\mathbf{r})$ due to the interaction of a point

TABLE I. Elastic constants from calculation in a unit cell.

Elastic constant	Value
C_{11}	299.5 GPa
C_{12}	233 GPa
C_{44}	133.6 GPa
S_{11}	1.046×10^{-2} GPa^{-1}
S_{12}	-4.58×10^{-2} GPa^{-1}
S_{44}	7.61×10^{-2} GPa^{-1}

defect at $\mathbf{r}$ with a strain field $\varepsilon_{ij}(\mathbf{r})$:

$$\Delta E(\mathbf{r}) = -\sum_{i,j} P_{ij} \varepsilon_{ij}(\mathbf{r}) - \frac{1}{2} \sum_{i,j,k,l} \varepsilon_{ij}(\mathbf{r}) \mathfrak{M}_{ijkl} \varepsilon_{kl}(\mathbf{r}), \tag{4}$$

where $\varepsilon_{ij}(\mathbf{r})$ is the total strain field at the location $\mathbf{r}$ due to both the point defect and any external stress. The total elastic energy E^{el} of a system of volume V containing a single point defect at $\mathbf{r}$ is then

$$E^{\text{el}} = \sum_{i,j,k,l} V \frac{1}{2} \varepsilon_{ij}(\mathbf{r}) C_{ijkl} \varepsilon_{kl}(\mathbf{r}) - \sum_{i,j} P_{ij} \varepsilon_{ij}(\mathbf{r})$$
$$- \frac{1}{2} \sum_{i,j,k,l} \varepsilon_{ij}(\mathbf{r}) \mathfrak{M}_{ijkl} \varepsilon_{kl}(\mathbf{r}), \tag{5}$$

where C_{ijkl} are the elastic constants of the host crystal. The first term on the right-hand side describes the bulk elastic energy of the host structure due to the total strain. The second and third terms describe the interaction between the point defect and the total strain. Hence, the elastic dipole is the linear response to strain of a system containing a point defect, which is given in the linear limit by the stress tensor of the system without volume or shape relaxation:

$$\underline{P} = -V \underline{\sigma}(\underline{\varepsilon}). \tag{6}$$

The elastic dipole reproduces the symmetries of the point defect it describes. A vacancy on a substitutional site of the fcc structure of a pure nickel crystal has a cubic symmetry: the elastic dipole is a scalar $\underline{P} = P\mathbb{1}$. It can be computed from the stress tensor of an unstrained DFT calculation of a defect. For a vacancy, we find $P = -6.33$ eV, and this value can be used to evaluate the vacancy relaxation volume $V_V = \frac{P}{K}$, where $K = \frac{1}{3}(C_{11} + 2C_{12})$ is the bulk modulus obtained from the elastic constant presented in Table I. A value $V_V = (-0.394 \pm 0.005) V_{\text{at}}$ of the vacancy relaxation volume, expressed in atomic volume, is found, in agreement with the experimental value $V_V = -0.4 V_{\text{at}}$ of Ref. [44] obtained by diffuse x-ray scattering.

In pure Ni, during an atom-vacancy exchange along the [011] direction, the saddle point configuration is monoclinic. Figure 2 illustrates this situation with the jump of a vacancy in the [110] direction. While the [100] and [010] directions of the crystal are equivalent in that case, the [001] direction is distinct. Hence, in the saddle point configuration the elastic dipole has the form

$$\underline{P} = \begin{pmatrix} P_{xx} & P_{yx} & 0 \\ P_{xy} & P_{yy} & 0 \\ 0 & 0 & P_{zz} \end{pmatrix}, \tag{7}$$

with $P_{yx} = P_{xy}$ and $P_{xx} = P_{yy}$. As a consequence, [001] strain will have a different effect than a [100] or a [010] strain on the frequency of an atomic jump in the [011] direction. Moreover, while shear strain does not affect the formation energy of a vacancy, it will affect its saddle point energy. The introduction of a solute atom further reduces the symmetry of the system unless it is placed on the axis of the solute-vacancy jump.

As the migration barrier is the difference between the enthalpy in the saddle point configuration and the enthalpy in the initial configuration, the first-order effect of strain on the migration barrier is the difference between the two elastic dipoles in the two configurations. This difference can be captured by two different methods. A first method is to compute a finite difference between the energies of two strained cells in both the initial and the saddle point configuration. Another method is to obtain the stress tensor in both the initial and the saddle point configurations on an unstrained cell, which is proportional to the elastic dipole according to Eq. (6). The diaelastic polarizability corresponds to the second derivative of the energy with respect to the strain. Thus, it cannot be evaluated by using the stress tensor of the unstrained cell. However, it can be evaluated by using a finite-difference approach. The drawback of finite-difference calculations is their CPU cost, as they require the use of both unstrained and strained cells. As a consequence, in the present work, finite-difference calculations are performed to determine the range of validity of the linear approximation, and the dependency of the migration barrier within that range is obtained using the stress tensor.

D. Finite-size bias

The elastic dipole and diaelastic polarizability, as they have been defined in this section, should be obtained by measuring the stress on a volume embedded in an infinite crystal. The periodic boundary conditions lead to interactions between the stress fields generated by a point defect and its periodic images. The impact of this bias has been evaluated by computing the elastic dipole in $2 \times 2 \times 2$ and $3 \times 3 \times 3$ supercells for different initial and saddle point configurations. Comparing calculations in $2 \times 2 \times 2$ supercells with calculations in $3 \times 3 \times 3$ supercells, the amplitude of the different component of the elastic dipole is systematically underevaluated by 10%. Due to their computational cost, no calculations could be conducted in supercells larger than $3 \times 3 \times 3$ to provide more accurate results. However, as shown in Ref. [45], the elastic dipoles converge as $1/V$, where V is the volume of the supercell. Thus, the finite-size error due to a use of a $3 \times 3 \times 3$ supercell can be estimated to remain below 5%.

III. DFT RESULTS

A. Diffusion of Si in Ni in the absence of strain

First, the migration frequencies have been computed in the unstrained case. Calculations were performed in the $3 \times 3 \times 3$ cell to obtain the binding energy E_d^B between the vacancy and a Si atom at a distance d in terms of nearest neighbors. Let $E^{108\text{Ni}}$, $E_{1\text{Si}}^{107\text{Ni}}$, $E^{107\text{Ni}}$, and $E_{1\text{Si},d}^{106\text{Ni}}$ be respectively the energy of a system of pure Ni, of a system containing a Si atom, of a system containing a vacancy, and of a system containing both;

TABLE II. Binding energies between the vacancy and the Si atom at different distances.

Distance	Binding energy (eV)
First NN	-0.108
Second NN	$+0.004$
Third NN	$+0.037$
Fourth NN	-0.008
Fifth NN	$+0.000$

the binding energy E_d^B is defined as the difference:

$$E_d^B = E_{1\text{Si},d}^{106\text{Ni}} + E^{108\text{Ni}} - E_{1\text{Si}}^{107\text{Ni}} - E^{107\text{Ni}}. \tag{8}$$

Even at the fourth-nearest-neighbor site, both the vacancy and solute share a common Ni neighbor. As shown in Table II, a nonnegligible binding energy is found between vacancies and solute atoms at first and third NN distance. Thus, 16 frequencies are required to describe flux couplings during the diffusion of Si impurities [4].

The migration barriers of the 16 frequencies have been computed and can be found in Table III, as well as the attempt frequencies corresponding to the seven of them starting or ending on a first-NN site. The difference between the attempt frequencies computed is below 10%. For jumps of a Ni atom from a first to a third NN sites of the Si atom or from a third-NN site to a first-NN site, the attempt frequency is similar to jumps in bulk nickel. As a consequence, attempt frequencies for more distant jumps were not computed and a value equal to that of the bulk is assumed. All the migration

TABLE III. Attempt frequencies and migration barriers of each atomic jump involved in the diffusion of dilute Si in Ni in the absence of stress obtained from direct DFT calculations [27] and using the LIMB approximation. Values with an asterisk * were considered to be far enough from the solute to match the bulk value and were not separately computed.

Event	Frequency	ν (THz)	E^{mig} (DFT) (eV)	E^{mig} (LIMB) (eV)
0	$w_1^{(0)}$	4.8	1.074	
1	$w_1^{(2)}$	5.1	0.891	
2	$w_{111}^{(1)}$	5.2	1.003	1.074
3	$w_{121}^{(1)}$	5.3	1.213	1.130
4	$w_{112}^{(1)}$	5.1	1.101	1.018
5	$w_{131}^{(1)}$	4.8	1.153	1.147
6	$w_{113}^{(1)}$	4.8	1.008	1.002
7	$w_{132}^{(1)}$	4.8*	1.091	1.091
8	$w_{123}^{(1)}$	4.8*	1.058	1.058
9	$w_{133}^{(1)}$	4.8*	1.089	1.074
10	$w_{1\infty1}^{(3)}$	4.8*	1.128	1.128
11	$w_{1\infty2}^{(3)}$	4.8*	1.066	1.072
12	$w_{1\infty3}^{(3)}$	4.8*	1.068	1.056
13	$w_{11\infty}^{(4)}$	4.8*	1.028	1.020
14	$w_{12\infty}^{(4)}$	4.8*	1.077	1.076
15	$w_{13\infty}^{(4)}$	4.8*	1.112	1.093

barriers of the vacancy-nickel atom exchanges are between 1.0 eV and 1.2 eV. However, the solute-vacancy exchange has a significantly lower migration barrier, which is consistent with the small size of Si atoms. These results can be used to test the validity of the linearly interpolated migration barriers (LIMB) approximation, introduced in Ref. [46] and also known as the kinetically resolved activation barrier approximation [47]. This approximation considers the perturbation to the bulk migration barrier due to the impurity to be the average of the binding energy in the initial and final configurations. The migration barrier associated with a frequency $w_{abc}^{(\zeta)}$ is thus given by

$$E_{abc}^{\mathrm{mig},(\zeta)} = E_a^{\mathrm{mig},(0)} + \tfrac{1}{2}\left(E_b^B - E_c^B\right), \qquad (9)$$

where $E_a^{\mathrm{mig},(0)}$ is the migration barrier for a jump in the same direction far from the solute. For a number of frequencies, this approximation appears in excellent agreement with the direct DFT results. However, for some frequencies such as $w_{111}^{(1)}$ or $w_{121}^{(1)}$, they disagree by more than 50 meV. As $w_{111}^{(1)}$ has a high impact on kinetic correlations [4], this disagreement can induce qualitative differences in the modeling of macroscopic kinetic properties and the linearly interpolated migration barriers should be avoided at least for jumps involving first-NN sites.

The jump frequencies can be used to compute the Onsager matrix and the diffusion coefficient of the solute impurities in the dilute limit [5]. The term D_{ij} of the diffusivity matrix related to the chemical species i and j is directly related to the Onsager matrix and the chemical potential

$$D_{ij} = \sum_k L_{ik}\frac{\partial \mu_k}{\partial c_j}, \qquad (10)$$

where the sum is performed over all the chemical species k, μ_k is the chemical potential related to k, and c_j is the concentration in j. In the dilute limit, the entropic contribution dominates in the derivative of the chemical potential; at a temperature T and an atomic volume V, the diffusion coefficient of silicon impurities is then

$$D_{\mathrm{SiSi}} = \frac{k_B T}{V}L_{\mathrm{SiSi}}, \qquad (11)$$

where L_{SiSi} is the silicon-related diagonal term of the Onsager matrix. The Onsager matrix is obtained with the self-consistent mean field method [3,48] by using the results in Ref. [4] where kinetic correlations are truncated beyond the third-NN sites of the third-NN sites. The diffusion coefficients obtained are presented in Fig 3. An excellent agreement with experimental Si diffusion coefficients is obtained, which confirms the validity of some of the DFT values: as this quantity is mostly sensitive to the vacancy formation energy, to the NN binding energy, and to the w_1^2 frequency, it cannot be used to confirm the values of the other frequencies. This also shows good agreement with our nonmagnetic treatment of Ni.

B. Effect of strain on the jump frequencies

1. Effect of the diaelastic polarizability

In order to evaluate the importance of the diaelastic polarizability, the finite-difference method has been used, applying the transformations defined in the Appendix to
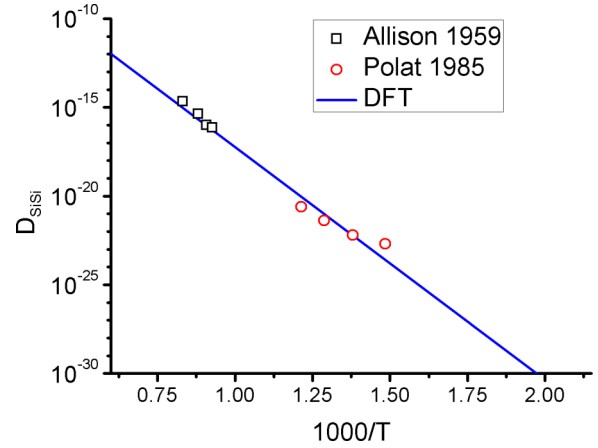
FIG. 3. (Color online) Diffusion coefficient of Si impurities in Ni as a function of the inverse temperature. Empty symbols are experimental results from Refs. [49,50] while the solid blue line is the result of the present work.

a $3 \times 3 \times 3$ cubic cell with $\delta = 0.01$. A comparison with the effect of strain as computed from the elastic dipole is performed. Figure 4 shows the effect of uniaxial strain on the migration barrier corresponding to the $w_1^{(0)}$ and the $w_1^{(2)}$ frequencies of jumps in the [110] direction, as computed by finite difference or by the elastic dipole. The two methods provide results in excellent agreement, indicating that no influence of the second order term could be captured by finite difference calculations. Similar calculations performed for the $w_{111}^{(1)}, w_{121}^{(1)}$, and $w_{112}^{(1)}$ frequencies confirmed this result. Hence, it appears that the diaelastic polarizability can be neglected for practical purpose in the Ni(Si) alloy and that finite difference calculation are not necessary for strains below $\delta = 1\%$ as all the relevant information is provided by the elastic dipole, which can be obtained by calculations on the unstrained cell.
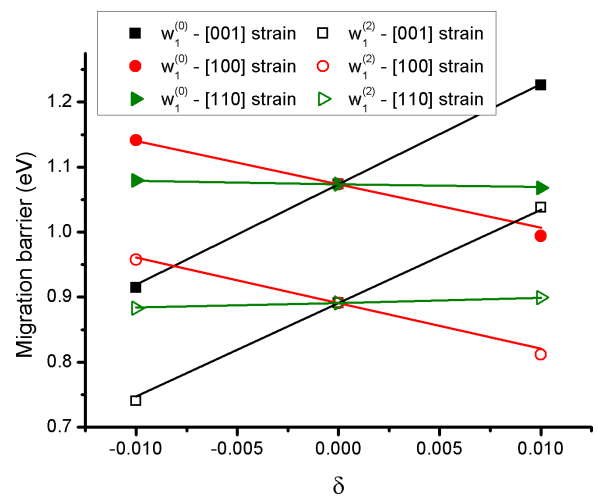
FIG. 4. (Color online) Migration barrier as a function of uniaxial strain. The filled (resp. hollow) symbols correspond to results obtained by finite-difference calculation for the frequency $w_1^{(0)}$ (resp. $w_1^{(2)}$). Solid lines show the slopes from the elastic dipole. Calculations were performed in a $3 \times 3 \times 3$ tetragonal cell under a uniaxial strain $\underline{\varepsilon}^u(\delta)$ either in the (100) or the (001) direction or a shear strain (110).
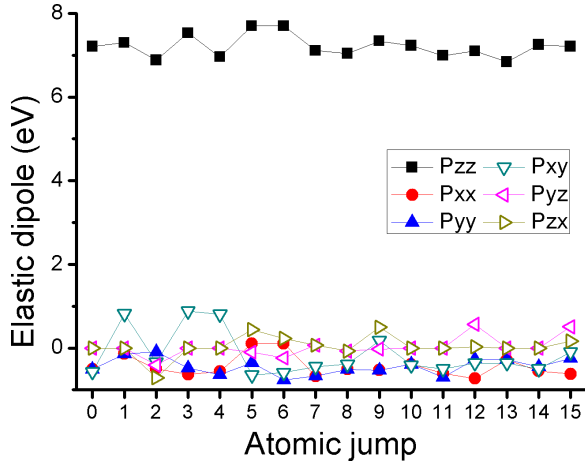
FIG. 5. (Color online) Values of the elastic dipole of the migration barrier for the 16 different exchanges corresponding to an atomic jump along the [110] direction ($x = [100]$, $y = [010]$, $z = [001]$).

FIG. 6. (Color online) Attempt frequencies as a function of a uniaxial strain $\underline{\varepsilon}^u(\delta)$ either along the [100] or the [001] direction for the frequencies $w_1^{(0)}$ and $w_1^{(2)}$. The solid lines correspond to linear fits.

2. Strain effect on the migration barriers

For any of the 16 different jumps in the [110] direction of the unstrained system, the difference of elastic dipole between the saddle point configuration and the initial configuration determines the effect of strain on the migration barriers [51]. The values of the six components of the elastic dipole of the migration barrier of each of the 16 different jump types are displayed in Fig. 5 for a jump vector $\frac{a}{2}[110]$. From these values, the effect of strain on jumps along different directions can be retrieved by rotation. As shown in Fig. 5 and in Table IV, the elastic dipole shows little variations from one jump to another. The strain dependency of the migration barrier thus seems to be mostly independent of the position of the Si solute atom. Moreover, the influence of shear strain on the migration barriers appears to be negligible compared to the influence of uniaxial strain. However, the jump direction has a large impact on the migration barrier. For example, in the presence of a strain tensor $\underline{\varepsilon}_{ij}$ without shear, an $w_1^{(0)}$ jump in the [110] direction will see a migration barrier $E_1^{\mathrm{mig},(0)}[110] = E_1^{\mathrm{mig},(0)} + P_{xx}\varepsilon_{11} + P_{yy}\varepsilon_{22} + P_{zz}\varepsilon_{33}$, where $E_1^{\mathrm{mig},(0)} = 1.074\mathrm{eV}$, $P_{xx} = P_{yy} = -0.51\mathrm{eV}$, and $P_{zz} = 7.20\mathrm{eV}$, while an $w_1^{(0)}$ jump in the [101] direction will see a migration barrier $E_1^{\mathrm{mig},(0)}[110] = E_1^{\mathrm{mig},(0)} + P_{yy}\varepsilon_{11} + P_{zz}\varepsilon_{22} + P_{xx}\varepsilon_{33}$.

TABLE IV. Elastic dipole of the migration barrier for a jump in the [110] direction: average value over the 16 frequencies and standard deviation.

Term	Average (eV)	Standard deviation (eV)
P_{xx}	-0.44	0.23
P_{yy}	-0.44	0.23
P_{zz}	7.21	0.26
P_{xy}	-0.16	0.53
P_{yz}	0.02	0.23
P_{xz}	0.04	0.26

3. Strain effect on the attempt frequencies

Similar to what has been presented for the migration barrier, the effect of strain on the attempt frequencies can be obtained by finite-difference calculations. Two frequencies, $w_1^{(0)}$ and $w_1^{(2)}$, are split in only two different frequencies by a uniaxial strain. Figure 6 shows the corresponding attempt frequencies obtained by finite-difference calculations in cells under a volume-conserving uniaxial strain $\underline{\varepsilon}^u(\delta)$. No contribution of the strain at the second order could be identified. Similar calculations performed for the $w_{111}^{(1)}, w_{121}^{(1)}$, and $w_{112}^{(1)}$ frequency confirmed this result. Thus, the effect of the diaelastic polarizability on the attempt frequencies was assumed to be negligible in all cases.

The impact of strain on the attempt frequencies has been investigated. For the five frequencies $w_1^{(0)}, w_1^{(2)}, w_{111}^{(1)}, w_{121}^{(1)}$, and $w_{112}^{(1)}$ that are split into 15 unique frequencies under a uniaxial strain, the attempt frequencies have been computed. The results, presented in Fig. 7, show that the effect of strain on the attempt frequencies remains limited in all cases, with a variation by less than 10% for a volume-conserving uniaxial strain $\underline{\varepsilon}^u(\delta)$ with $\delta = 0.01$. At temperatures below the melting point the jump frequencies are mostly controlled by the migration barriers; hence the effect of strain on the attempt frequencies is of little consequence and can be neglected for the calculation of strain effects on the diffusion properties of Ni(Si).

IV. ELASTIC CAGE MODEL

In Ref. [30], Ardell and Prikhodko proposed a model of stress effect on the migration barrier for vacancy-atom exchanges in pure metals based on the so-called dynamical theory of atom migration [52]. This model assumes that the effect of stress on the migration is due to the strain that the jumping atom induces in the saddle point position to atoms of the "cage" surrounding the saddle point. The DFT results obtained in this study can be used to evaluate the ability of this model to predict the effect of strain on $E_1^{(0)}$.
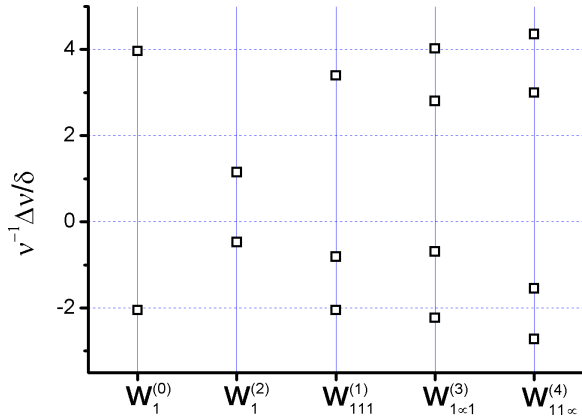
FIG. 7. (Color online) Relative variations of the attempt frequencies with the amplitude of a uniaxial strain for the five frequencies $w_1^{(0)}, w_1^{(2)}, w_{111}^{(1)}, w_{121}^{(1)}$, and $w_{112}^{(1)}$ numbered from 0 to 4. The different values for a given atomic jump correspond to different orientations of the jumping atom-solute-vacancy triangle with respect to the direction of the strain.

During a jump along the [110] direction, at the saddle point, the jumping atom passes through a rectangular "cage" of 4 atoms of dimension a in the [001] direction and $a/\sqrt{2}$ in the [1$\bar{1}$0] direction as illustrated in Fig. 2. The diagonals of this cage are the dense directions of the saddle point configuration, and its length is affected by strain. Considering the volume-conserving uniaxial strain $\underline{\varepsilon}^u(\delta)$ along the z direction detailed in the Appendix, the length of the diagonal changes by -2δ, while under a [100] or [010] uniaxial strain, the diagonal length increases by δ. An increase of the saddle point energy under a strain along the z direction, and a proportional decrease for a [100] or [010] strain, can thus be expected. Similarly, while a [101] or a [011] shear strain does not affect the plane of the cage at first order, the [110] shear strain contracts the diagonals of the cage by δ, and an increase of the migration barrier can be expected for jumps along the [110] direction, together with a decrease for exchanges along the [1$\bar{1}$0] direction. These situations are illustrated in Fig. 8. As a consequence, the overall effect of strain on the jump frequencies highly depends on the orientation of the jump with respect to the strain as already observed in Sec. III B.

In the model of Ardell and Pridkhodko, by considering the displacement of the atoms forming that cage, the variation of the migration barrier with stress can be computed from the elastic constants of the bulk crystal. Considering the diffusion of a vacancy in bulk nickel under a uniaxial strain along the [001] direction, the ratio of the variation $\Delta E_{[110]}^{\text{mig}}$ of strain on the migration barrier of a jump in the [110] direction against the variation $\Delta E_{[011]}^{\text{mig}}$ of the migration barrier of a jump in the [011] direction is then according to this model

$$\frac{\Delta E_{(110)}^{\text{mig}}}{\Delta E_{(011)}^{\text{mig}}} = -\frac{8C_{11} + 22C_{12}}{7C_{11} + 8C_{12}}. \tag{12}$$

To a stress σ in the [001] direction corresponds a strain $S_{11}\sigma$ in the [001] direction and a strain $S_{12}\sigma$ in the [100] and [010]
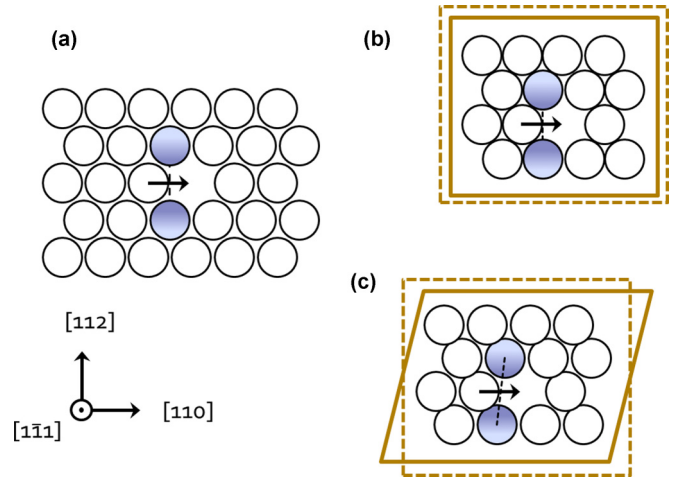
FIG. 8. (Color online) Representation of the (1$\bar{1}$1) plane during an atomic jump in the [110] direction in the absence of external strain (a), in the presence of strain in the [100] direction (b), and in the [001] direction (c). The filled circles are the nearest atom of the saddle point and the dashed line between them emphasizes the cage diagonal; the dashed boxes represent an area of the [111] plane before strain while the solid boxes represent that same area after strain.

direction. Thus the ratio in Eq. (12) can also be written

$$\frac{\Delta E_{[110]}^{\text{mig}}}{\Delta E_{[011]}^{\text{mig}}} = -\frac{P_{zz}S_{11} + S_{12}(P_{xx} + P_{yy})}{P_{yy}S_{11} + S_{12}(P_{xx} + P_{zz})}. \tag{13}$$

This model can be tested using the DFT results on Ni. The elastic constants have been computed on a $1 \times 1 \times 1$ supercell and the compliances are derived from them (see Table I). The ratio of Eq. (13) is computed using the elastic dipole $\frac{\Delta E_{[110]}^{\text{mig}}}{\Delta E_{[011]}^{\text{mig}}} = -2.2$, and is in good agreement with the value $\frac{\Delta E_{[110]}^{\text{mig}}}{\Delta E_{[011]}^{\text{mig}}} = -1.9$ predicted using Eq. (12) from the model of Ardell and Prikhodko [30]. However, this model is currently limited to the case of pure systems, and no comparison could thus be performed in the case of the Ni-Si alloy.

V. CONCLUSION

In this work, DFT calculations have been performed to study the effect of stress on the diffusion of Si impurities in Ni by the vacancy-mediated mechanism. Using crystal symmetry, the effect of a uniaxial and a shear strain only needs to be computed to obtain the effect of an arbitrary strain in the linear limit. In the case of the Ni(Si) alloy, second-order effects of stress are measured to be negligible, justifying this approach.

Strain induces a splitting of the different migration events involved in the diffusion of a dilute substitutional solute. Hence, the study of the effect of a given strain tensor on diffusion requires the knowledge of all the split migration frequencies. However, explicit calculation of all the migration enthalpies and attempt frequencies using strained cells proved to be unnecessary, as the elastic dipole for the different migration events on unstrained cells quantified the effect of strain on the migration barriers. While this method could not be applied to the attempt frequencies, their lesser influence on the migration frequency and their limited dependency on

strain allowed neglecting the effect of strain on them. Thus, only a reduced number of attempt frequencies calculation are required.

In pure Ni, the effect of strain found from DFT calculations shows good agreement with a simple elastic model proposed in Ref. [30]. In the presence of Si impurities, the effect of strain on vacancy migration appears to be notably independent from the position of the Si impurities. However, nothing indicates that this property could be generalized to other impurities.

ACKNOWLEDGMENTS

APPENDIX A: STRAINED-CELL GEOMETRIES

In addition to the unstrained cubic geometry, three different geometries have been studied: two volume-conserving ones associated respectively with uniaxial and shear strains, and one under volumetric strain to determine the effect of elementary strains by finite difference. Starting from the relaxed cell, the following stress tensor is used for calculation under volumetric strain:

$$\underline{\varepsilon}^{v}(\delta) = \begin{pmatrix} \delta & 0 & 0 \\ 0 & \delta & 0 \\ 0 & 0 & \delta \end{pmatrix}. \qquad (A1)$$

Similarly, the volume-conserving strain tensor for uniaxial strain relative to the cube axes $\langle 001 \rangle$ used in the calculations is given by

$$\underline{\varepsilon}^{u}(\delta) = \begin{pmatrix} \delta & 0 & 0 \\ 0 & \delta & 0 \\ 0 & 0 & (\delta+1)^{-2} - 1 \end{pmatrix}. \qquad (A2)$$

This strain tensor lowers the symmetry of fcc Ni (space group 225) to BCT (space group 139). Finally, the following stress tensor is used for calculation under shear strain:

$$\underline{\varepsilon}^{s}(\delta) = \begin{pmatrix} 0 & \delta/2 & 0 \\ \delta/2 & 0 & 0 \\ 0 & 0 & \frac{(\delta/2)^2}{1-(\delta/2)^2} \end{pmatrix}. \qquad (A3)$$

[1] W. G. Wolfer, in *Comprehensive Nuclear Materials*, edited by R. J. M. Konings (Elsevier, Amsterdam, 2012), pp. 1–45.

[2] J. Philibert, *Atom Movements: Diffusion and Mass Transport in Solids* (EDP Science, France, 1991).

[3] T. Garnier, M. Nastar, P. Bellon, and D. R. Trinkle, Phys. Rev. B **88**, 134201 (2013).

[4] T. Garnier, D. R. Trinkle, M. Nastar, and P. Bellon, Phys. Rev. B **89**, 144202 (2014).

[5] A. R. Allnatt and A. B. Lidiard, *Atomic Transport in Solids* (Cambridge University Press, Cambridge, 1993).

[6] Z. Jiao and G. Was, Acta Mater. **59**, 1220 (2011).

[7] A. Barbu and G. Martin, Scr. Metall. **11**, 771 (1977).

[8] A. Barbu, G. Martin, and A. Chamberod, J. Appl. Phys. **51**, 6192 (1980).

[9] G. Martin, Phys. Rev. B **30**, 1424 (1984).

[10] M. Nastar and F. Soisson, in *Comprehensive Nuclear Materials*, edited by R. J. M. Konings (Elsevier, Amsterdam, 2012), pp. 471–497.

[11] A. Barbu and A. J. Ardell, Scr. Metall. **9**, 1233 (1975).

[12] Z. Mao, C. K. Sudbrack, K. E. Yoon, G. Martin, and D. N. Seidman, Nat. Mater. **6**, 210 (2007).

[13] F. Soisson and C. C. Fu, Phys. Rev. B **76**, 214102 (2007).

[14] J. Tucker, R. Najafabadi, T. Allen, and D. Morgan, J. Nucl. Mater. **405**, 216 (2010).

[15] M. Mantina, Y. Wang, L. Chen, Z. Liu, and C. Wolverton, Acta Mater. **57**, 4102 (2009).

[16] A. Van der Ven and G. Ceder, Phys. Rev. Lett. **94**, 045901 (2005).

[17] F. Larche and J. Cahn, Acta Metall. **30**, 1835 (1982).

[18] M. P. Puls and C. H. Woo, J. Nucl. Mater. **139**, 48 (1986).

[19] E. Clouet, Acta Mater. **54**, 3543 (2006).

[20] E. Clouet, S. Garruchet, H. Nguyen, M. Perez, and C. S. Becquart, Acta Mater. **56**, 3450 (2008).

[21] E. J. Savino, Philos. Mag. **36**, 323 (1978).

[22] P. H. Dederichs and K. Schroeder, Phys. Rev. B **17**, 2524 (1978).

[23] C. Woo, J. Nucl. Mater. **120**, 55 (1984).

[24] V. Vaithyanathan, C. Wolverton, and L. Q. Chen, Phys. Rev. Lett. **88**, 125503 (2002).

[25] C. N. Tomé, H. A. Cecatto, and E. J. Savino, Phys. Rev. B **25**, 7428 (1982).

[26] R. G. A. Veiga, M. Perez, C. S. Becquart, C. Domain, and S. Garruchet, Phys. Rev. B **82**, 054103 (2010).

[27] T. Garnier, V. R. Manga, D. R. Trinkle, M. Nastar, and P. Bellon, Phys. Rev. B **88**, 134108 (2013).

[28] R. G. A. Veiga, M. Perez, C. Becquart, E. Clouet, and C. Domain, Acta Mater. **59**, 6963 (2011).

[29] C. Varvenne, F. Bruneval, M.-C. Marinica, and E. Clouet, Phys. Rev. B **88**, 134102 (2013).

[30] A. Ardell and S. Prikhodko, Acta Mater. **51**, 5013 (2003).

[31] G. Vineyard, J. Phys. Chem. Solids **3**, 121 (1957).

[32] G. Kresse and J. Hafner, Phys. Rev. B **47**, 558(R) (1993).

[33] G. Kresse and J. Furthmuller, Phys. Rev. B **54**, 11169 (1996).

[34] J. P. Perdew and A. Zunger, Phys. Rev. B **23**, 5048 (1981).

[35] P. Ehrhart, *Atomic Defects in Metals* (Springer-Verlag, Berlin, 1991), p. 88.

[36] T. R. Mattsson and A. E. Mattsson, Phys. Rev. B **66**, 214110 (2002).

[37] K. Carling, G. Wahnstrom, T. R. Mattsson, A. E. Mattsson, N. Sandberg, and G. Grimvall, Phys. Rev. Lett. **85**, 3862 (2000).

[38] G. Henkelman, B. Uberuaga, and H. Jónsson, J. Chem. Phys. **113**, 9901 (2000).

[39] S. Wei and M. Y. Chou, Phys. Rev. Lett. **69**, 2799 (1992).

[40] W. Frank, C. Elsässer, and M. Fähnle, Phys. Rev. Lett. **74**, 1791 (1995).

[41] A. van de Walle, Alloy Theoretic Automated Toolkit, http://www.its.caltech.edu/~avdw/atat.

[42] A. van de Walle, Calphad **33**, 266 (2009).

[43] *Structure Data of Elements and Intermetallic Phases*, edited by P. Eckerlin, H. Kandler, and A. Stegherr, Landolt-Börnstein, New Series, Group III, (Springer-Verlag, Berlin, 1971) Vol. 6.

[44] O. Bender and P. Ehrhart, J. Phys. F **13**, 911 (1983).

[45] B. Puchala, M. L. Falk, and K. Garikipati, Phys. Rev. B **77**, 174116 (2008).

[46] A. Senhaji, G. Treglia, B. Legrand, N. Barrett, C. Guillot, and B. Villette, Surf. Sci. **274**, 297 (1992).

[47] A. Van der Ven, G. Ceder, M. Asta, and P. D. Tepesch, Phys. Rev. B **64**, 184307 (2001).

[48] M. Nastar, V. Y. Dobretsov, and G. Martin, Philos. Mag. **80**, 155 (2000).

[49] H. Allison and H. Samelson, J. Appl. Phys. **30**, 1419 (1959).

[50] S. Polat, C. Marsh, H. Chen, and J. Epperson, J. Met. **37**, A128 (1985).

[51] DFT data are available at http://hdl.handle.net/11115/239 through http://NIST.matDL.org.

[52] C. Flynn, *Point Defects and Diffusion* (Oxford University Press, Oxford, 1972).